MISSING FIGURES VOLUME I

On the following pages are figures that were unfortunately not reproduced during the first printing of Volume I. Our apologies to the authors for our error.

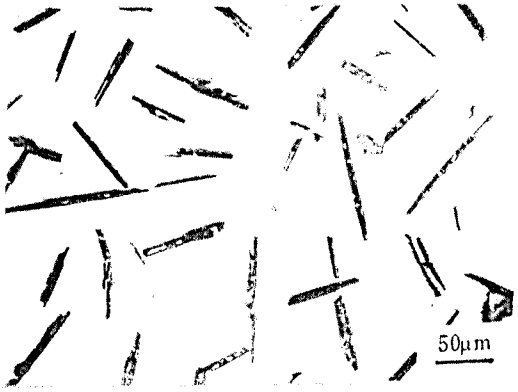

Fig. 1. Microstructure of Al—Cu—P alloy by optical observation

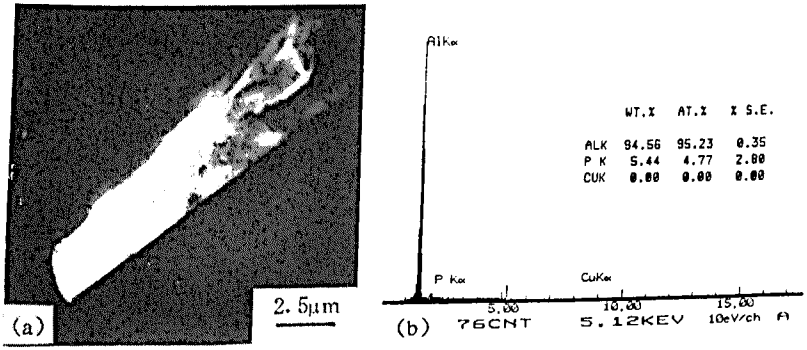

Fig. 2. Observation results of bar—shaped particle from,
(a) SEM morphology (b) EDAX analysis

Examination of Refining Effect

The microstructures of modified and unmodified Al—18%Si binary alloy are given in Fig. 3. In the unmodified alloy the coarse faceted primary silicon crystals were present and their distribution and size were hetergenous. In contract, in the modified alloy by Al—Cu—P alloy the primary silicon crystals were obviously small and their distribution were more homogenous. The results of the experiment indicated that when the content of P addition by Al—Cu—P alloy were changed from 10ppm to 80ppm, the average size of primary silicon would change from 40μm to 25μm. Fig. 4 shows the influence of P content on the average size of primary silicon. It is clear that the average size of primary silicon de creases with increasing content of P addition and the average

atoms, the Mn atom depletion occurred in the unsolidified zone. Therefore, the local composition of remaining liquid would shift back toward L+α-Al region. As the α-Al precipitated, the Mn atoms re-enriched in the finally solidified zone. As soon as the solid solubility limit of Mn in α-Al was reached, the eutectic-like reaction $L \rightarrow \alpha\text{-Al}+Al_6Mn$ occurred, and the Al_6Mn displayed plate-like structure. Then, the remaining liquid shifted back toward L+α-Al phase region again, and the Mg atoms continued to enrich in the interface front. Finally, as the solid solubility of Mg in growing α-Al was reached, the eutectic reaction $L \rightarrow \alpha\text{-Al}+Al_8Mg_5$ occurred and terminated the solidification process. Since the precipitation of Al_6Mn did not consume Mg atoms, the fraction of the eutectic compound Al_8Mg_5 was not affected by the Mn addition. Obviously, the influence of Mn addition on the solidification behavior of Al-Mg alloys was different from that of Cu addition. The solidification sequence of alloy II-2 was summarized as $L \rightarrow Al_6Mn+L_1 \rightarrow Al_6Mn+\alpha\text{-Al}+L_2 \rightarrow Al_6Mn+\alpha\text{-Al}+$plate-like $Al_6Mn+L_3 \rightarrow Al_6Mn+\alpha\text{-Al}+$plate-like $Al_6Mn+Al_8Mg_5$.

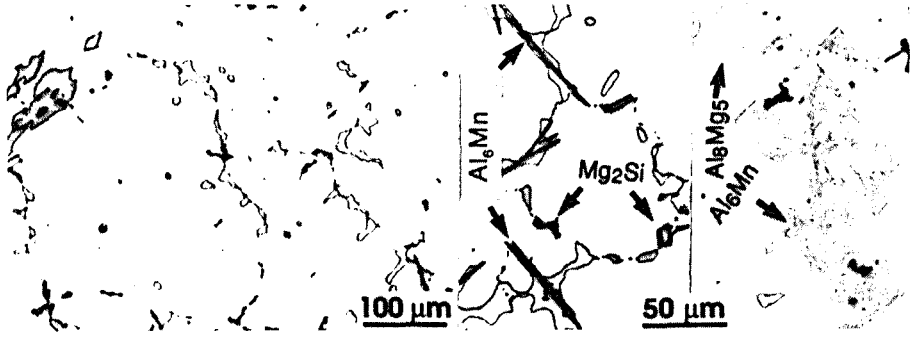

Fig.6 The microstructures of alloy II-2

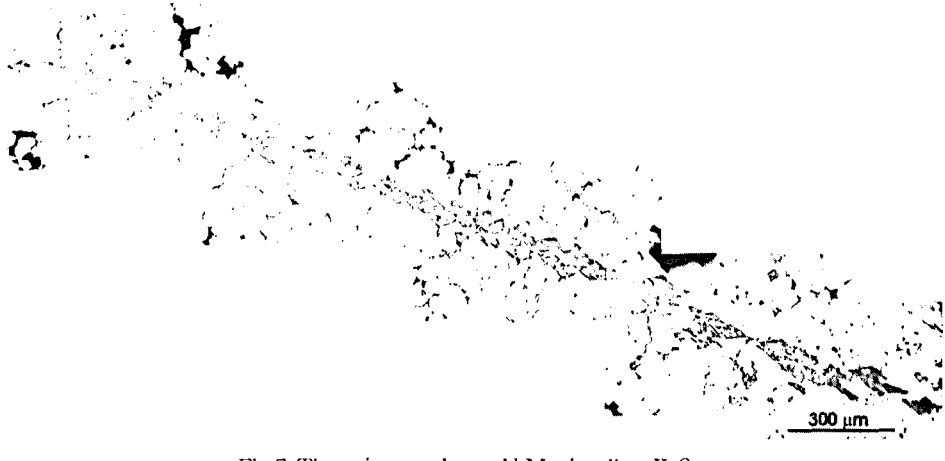

Fig.7 The primary phase Al_6Mn in alloy II-2

sion as the average diameter of the silver particles (1 μm). It is noted that hydrogen atoms are adjacent to the grain boundaries (Fig. 8a) and are present inside a grain (Fig. 8b). Silver particles were not observed at the grain boundaries on wider autoradiographs. It is thought that hydrogen atoms in the Al-Mg alloys diffuse to grain boundaries during deformation at high temperatures, and that they enhance the formation and growth of cavities at grain boundaries. It would be necessary to investigate the distribution of hydrogen in the alloy strained at high temperatures, while such experiments are considered to be very difficult to undertake on account of limited use of tritium.

Autoradiographs for the Al-Mg-Y alloy are shown in Fig 9. Figures 9A-C are magnified images of the regions designated by "A-C" in the left-hand photo, respectively. The small white particles, some of which are indicated by "Y," are yttrium-bearing compounds, and the large white ones indicated by the arrows are silver particles. Yttrium was present as yttrium-bearing compounds in the ingot, and the compounds were broken into many parts during free-forging. The broken parts have been aligned in the working direction. From these autoradiographs, it can be seen that hydrogen atoms in the Al-Mg-Y alloy are adjacent to yttrium-bearing compounds: presumably hydrogen atoms are present within the compounds or at the interfaces between the compounds and the matrix. Thus, it can be concluded that hydrogen atoms in the Al-Mg-Y alloy are trapped by yttrium-bearing compounds also during pre-stretching at 275°C and that formation and growth of cavities at grain boundaries are inhibited.

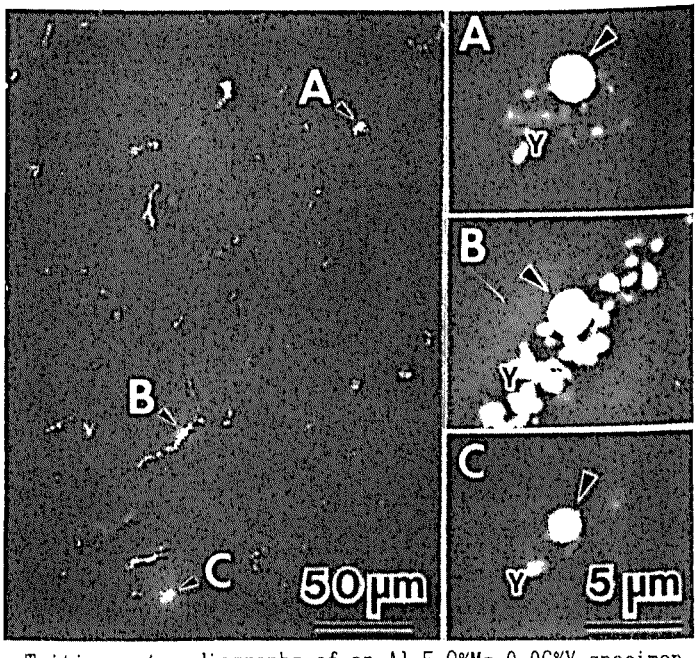

Figure 9. Tritium autoradiographs of an Al-5.9%Mg-0.06%Y specimen. Exposure time is 1.33Ms.

intermetallics in the middle. A tilted view after fracture allowed verification that the assumed initiation sites were the actual ones. On the same sample several initiation sites might be generated and it seems that microcracks appear rather lately. Indeed, the ratio of the crack initiation cycle number over the rupture cycle number seems to be greater than 0.8 .

Crack growth. From a macroscopical point of view the crack propagation occurs in mode I (Figure 4). However, locally the crack path, revealed by chemical etching, can have a zigzag shape following intergranular, transgranular, inter-subgranular or even sometimes trans-subgranular path (see for example figure 5). The intergranular path may be either along recrystallized/recrystallized grain boundaries or recrystallized/unrecrystallized grain boundaries. So, according to the microstructure all local fatigue crack paths are possible.

Percolation phenomenon. Since several macrocracks can exist the question is whether only one crack grows up leading to the final rupture or the macrocracks join together. All the macrocracks were observed on the surfaces of a sample before rupture in order to be able to follow their propagation. After rupture, the fracture surface profile showed that two macrocracks joined together. In addition, fractography observations showed two distinct initiation sites.

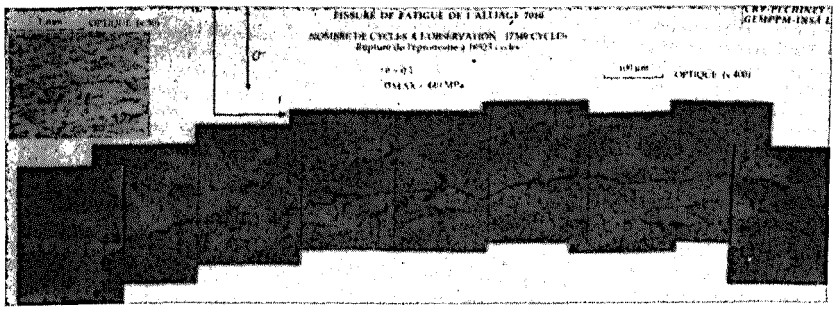

Figure 4. A long fatigue crack observed on the sample surface at N=17349 cycles (Nr = 18523 cycles)

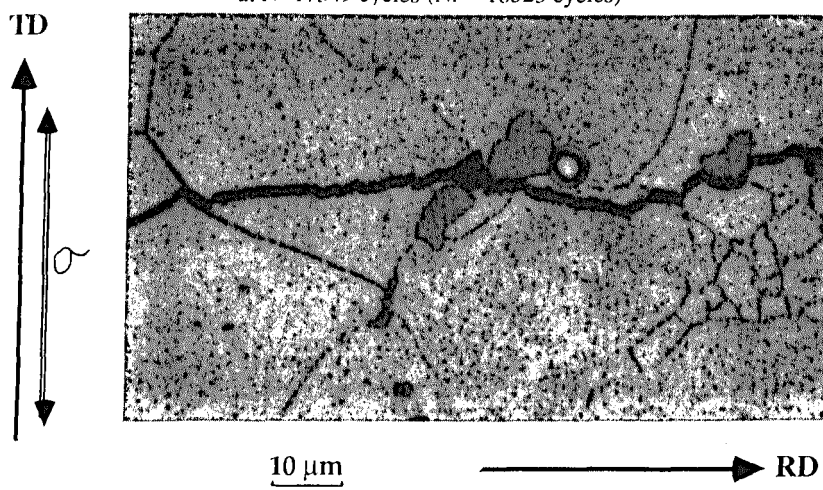

Figure 5. Detail of figure 4 showing the crack iniation site and local crack paths